Adaptive Simultaneous Topography and Broadband Nanomechanical Mapping of Heterogeneous Materials on Atomic Force Microscope

Tianwei Li[1], Qingze Zou[2,⋆], Tianxing Ma[3], Jonathan Singer[4], Chanmin Su[5]

***Abstract*—In this paper, an approach is proposed to achieve simultaneous imaging and broadband nanomechanical mapping of heterogeneous soft materials in air by using atomic force microscope (AFM). Simultaneous imaging and mechanical mapping (SIMM) is developed to, for example, correlate morphological and mechanical evolutions of the samples together. Current methods, however, are limited to nanomechanical mapping at a single frequency a time, or at frequencies much higher than those of interests for majority of soft polymers and live biological species. These limitations have been tackled through the recently-developed simultaneous imaging and broadband nanomechanical mapping (SIBNM) technique for materials of relatively small mechanical spatial variations. We propose, in this work, to extend the SIBNM technique to heterogeneous materials by developing a gradient-based adaptive Kalman-filtering technique to account for spatial variations of the sample mechanical properties when decoupling the sample topography tracking and the nanomechanical mapping from each other. A compressed-sensing technique is introduced to adaptively tune the gain of the adaptive Kalman filter. Experimental implementation of the proposed approach shows that both the topography imaging and the broadband mechanical mapping of heterogeneous soft samples can be reliably quantified.**

***Index Terms*—atomic force microscope imaging, nanomechanical mapping, adaptive Kalman filter, compressed sensing, iterative learning control**

I. Introduction

In this paper, the problem of simultaneous (topography) imaging and mechanical mapping (SIMM) of heterogeneous materials using atomic force microscope (AFM) is addressed. By combining two of the most important functions/operations of AFM, i.e., topography imaging and nanomechanical mapping, into one, SIMM not only dramatically improves the efficiency of AFM, but more importantly, provides the potential to quantitatively correlate and link the spatial variations of topography and mechanical properties of the sample together. Such a topography-mechanical correlation is needed and becomes a powerful tool in various areas, ranging from nano-/bio-material analysis and synthesis [1], nanomechanics [2], to biomechanics of live cells [3]. Specifically, continuous acquisition of time-elapsed topography-mechanical correlations is needed in interrogating dynamic evolutions of the sample at nanoscale, for example, in correlating morphological and rheological evolutions of live cell during the epithelial-mesenchymal transition process [4]. Such a real-time topography-mechanical correlation, however, is challenging and has not yet been satisfactorily achieved, particularly for soft heterogeneous materials.

Limitations exist in current techniques for SIMM. For example, the force-volume mapping method [5][6] has been widely used to map elastic modulus of the sample by continuously applying force curves of constant loading/unloading rate while scanning the sample in a raster pattern. Although mapping of the frequency-dependent modulus of the material can be obtained by changing the force load rate, the force load rate is limited to low frequency range (a few hundred Hz), and the mapping is limited to one frequency a time. The force load rate is increased in peak force [7] and other similar techniques (e.g., pulsed force [8] and fast force [9]). However, only single-frequency excitation force can be applied during the mapping process—to cover the viscoelasticity of the sample over a frequency range, the mapping needs to be repeated at each measurement frequency in that range. As a result, it is not only time consuming to cover a relatively broad frequency range, but also the repeated mappings tend to induce damage/deformation to soft samples such as live cells. Similar limitations also exist in the force modulation technique [10][11], its recent extension—the AFM-nDMA technique [12], and those mapping techniques based on tapping-mode imaging [13][14]. Although the mapping speed is increased in the tapping-mode based approach [13][14], the excitation force frequencies are not only limited (to one or two frequencies), but also are in the region (over tens of kHz to a few hundred kHz) much higher than that of most interests to the majority of polymers and biological samples. Therefore, techniques are needed to achieve rapid broadband nanomechanical mapping with simultaneous topography imaging.

These limitations, in both the measurement time and frequency range and simultaneous topography imaging, have

[1]Tianwei Li is a PhD candidate in the Department of Electrical and Computer Engineering, Rutgers University, Piscataway, NJ 08854, USA tianwei.li@rutgers.edu

[2]Qingze Zou is with the Department of Mechanical and Aerospace Engineering, Rutgers University, Piscataway, NJ 08854, USA qzzou@rci.rutgers.edu

[3]Tianxing Ma is a PhD candidate in the Department of Mechanical and Aerospace Engineering, Rutgers University, Piscataway, NJ 08854, USA tianxing.ma@rutgers.edu

[4]Jonathan Singer is with the Department of Mechanical and Aerospace Engineering, Rutgers University, Piscataway, NJ 08854, USA jonathan.singer@rutgers.edu

[5]Chanmin Su is with Shenzhen Academy of Robotics, Shenzhen 518000 China chanmin_su@yahoo.com

⋆ Author to whom any correspondence should be addressed.

been tackled through the recently developed simultaneous imaging and broadband nanomechanical mapping (SIBNM) technique [15]. The main idea is to inject a broadband excitation force into contact-mode AFM imaging, and integrate Kalman-filtering and an online iterative-learning feedforward-feedback control together [15]. Not only can topography imaging and nanomechanical mapping of the sample be obtained simultaneously, but also the viscoelasticity of the sample over a large frequency range can be obtained in one mapping process. Moreover, the measurement frequency can be chosen arbitrarily within a broad frequency region, ranging from a few Hz to a few kHz, thereby, covering the frequency range of most interests for soft polymers and live biological samples [2][4]. The SIBNM technique, however, has been developed for materials of relatively small mechanical spatial variations. Thus, SIMM of heterogeneous materials is yet to be achieved.

For heterogeneous materials, the effect of mechanical variations across the sample surface is pronounced and must be accounted for. During SIMM, the AFM response to the sample topography variation and that to the injected excitation signal (for mechanical mapping) are mixed and coupled together. Such a mixture might be avoided by clearly separating these two effects in the frequency domain as in the tapping-mode based techniques and its extensions [16][17]—by setting the spectrum of the excitation force at frequencies orders of magnitude higher than those in topography variations. As discussed above, however, these separation-based methods face fundamental limitations in the frequency range that can be measured. Instead, the mixed (cantilever deflection and z-piezo displacement) signals can be decoupled by using the Kalman-filtering technique, i.e., by utilizing, in the filtering process, the dynamics model from the cantilever to the probe-sample interaction [18][19]. This dynamics-model-based approach has been demonstrated experimentally on homogeneous polymer samples with pronounced topography variations [15]. For heterogeneous materials, however, additional issues arise as the underline dynamics (from the cantilever to the probe-sample-interaction) varies during the scanning, and such a dynamics variation becomes substantial over the entire imaging/mapping area. As a result, the conventional Kalman filter–based on a *fixed* cantilever-to-probe-sample-interaction dynamics model—becomes ineffective in discerning the mixed responses. Although the effect of the sample variation might be accounted for by using the extended Kalman filtering and unscented Kalman filtering techniques [20], such an extension is complicated as the spatial distribution of the sample mechanical properties—exactly what needs to be measured—is, in general, unknown a priori. Therefore, challenges exist in SIMM of heterogeneous materials.

In this paper, we propose an adaptive Kalman-filtering-based approach to achieve SIBNM of heterogeneous soft materials. Built upon the SIBNM approach [15], a gradient based method is proposed to adjust the gain of the Kalman filter online to accommodate the mechanical variations of the sample during the scanning. The key idea is to capture and exploit the mechanical variation of the sample on the first scan line to adaptively adjust the Kalman filter gain. Specifically, we introduce a compressed-sensing-based technique [21] to obtain the mechanical profile on the first scan line efficiently. The proposed approach is illustrated through experiment on a polydimethylsiloxane-epoxy (PDMS-epoxy) sample of both pronounced topography variation and significant heterogeneous mechanical properties, as well as a photocrosslinked epoxy sample with subtle mechanical and topographic differences. The results show that both the topography imaging and qualitative broadband mechanical mapping of the heterogeneous samples can be reliably obtained by using the proposed adaptive SIBNM technique.

The rest of the paper is organized as follows. In section II, the adaptive SIBNM technique is proposed with the application of an adaptive Kalman filter and the corresponding indicator recovered by compressed sensing. In section III, the experiment implementation and results are described and analyzed, respectively. Conclusions are commented in section IV.

II. Adaptive Simultaneous Topography and Broadband Nanomechanical Mapping

A. Overall scheme

Through the proposed approach, we aim to achieve, for soft heterogeneous materials, simultaneous topography imaging and nanomechanical mapping using AFM. The proposed approach is built upon, and extends the SIBNM technique recently developed for soft materials of relatively small spatial mechanical variations [15]. For heterogeneous materials, however, challenges arise as the mechanical properties of those samples can vary substantially across the sample surface.

The overall scheme of the proposed adaptive SIBNM (A-SIBNM) technique is depicted in Fig. 1. To excite the mechanical response of the sample, a broadband excitation signal (e.g., a multi-sinusoidal signal) is injected as feedforward signal (the "①-PBE signal" in Fig. 1) into the z-axis feedback loop for sample topography tracking (see Fig. 2), which in turn, allows mapping of the mechanical properties during the imaging. As such, both the z-axis piezo displacement ("②-$z_{sen,k}(j\omega)$" in Fig. 1) and the cantilever deflection ("③-$d_k(j\omega)$" in Fig. 1) consist of the response to the sample topography and that to the PBE input mixed together, respectively [15]. To account of the heterogeneous nature of the sample material, a gradient-based adaptive Kalman filter (see "Adaptive Kalm$_d(j\omega)$" in Fig. 1) is developed below to split the cantilever deflection signal into the response to the sample topography variation ("④-$d_{tp,k}(j\omega)$" in Fig. 1) and that to the PBE signal ("⑤-$d_{ind,k}(j\omega)$" in Fig. 1), respectively, which, in turn, are used for the feedback control of the sample topography tracking ("⑥-$G_{FB}(j\omega)$" in Fig. 1) and the generation of the nanomechanical mapping ("⑦-mechanical mapping" block in Fig. 1), respectively. The z-axis displacement is decoupled by using a Kalman filter ("⑧-Kalm$_z(j\omega)$" in Fig. 1) as the dynamics from the

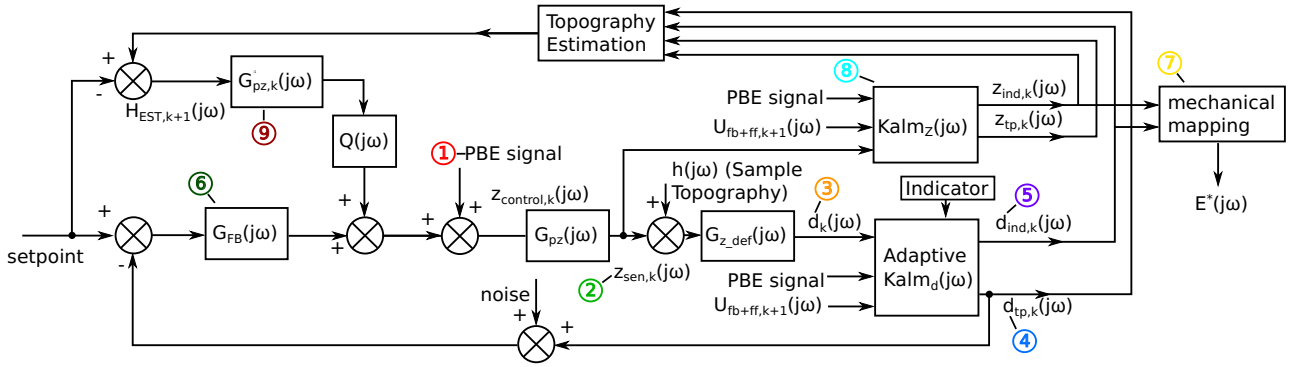

Fig. 1: Schematic block diagram of the proposed A-SIBNM approach, where the colored numbers mark out the signals and systems described in the text in the order of their first appearance, respectively.

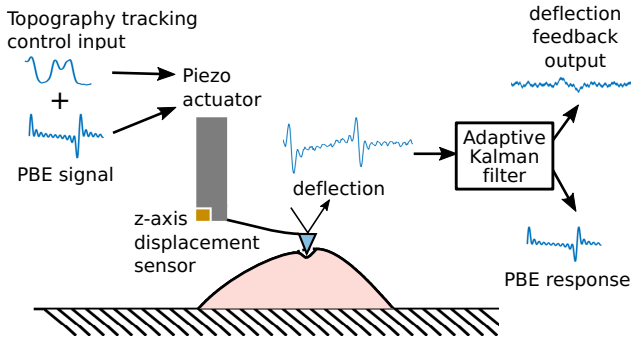

Fig. 2: Basic idea of the proposed A-SIBNM scheme where a periodic broadband excitation signal (PBE signal) is augmented and injected to the sample topography tracking signal for nanomechanical mapping while imaging simultaneously.

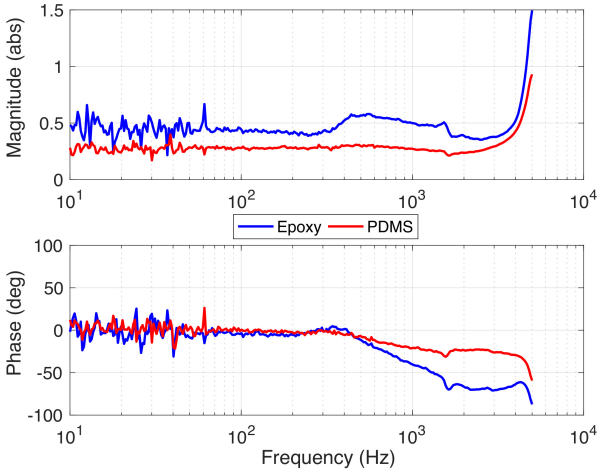

Fig. 3: Experimentally measured piezo-to-deflection frequency response (from the input voltage to the z-axis piezo actuator to the cantilever deflection) on (red) a PDMS sample and that on (blue) an epoxy sample, respectively.

piezo to the cantilever fix end is not sample dependent and remains the same during the imaging/mapping. Finally, a model-based approach is applied to estimate the indentation generated by the PBE signal ("Topography Estimation" block in Fig. 1), and a data-driven iterative feedforward control ("⑨-$G_{pz,k}(j\omega)$" and "$Q(j\omega)$" blocks in Fig. 1) is augmented to the feedback control of the z-axis to track the sample topography, respectively.

In the proposed A-SIBNM approach, key to addressing the heterogeneous effect of the sample is the gradient-based adaptive Kalman filtering, as presented next.

B. Gradient-based adaptive Kalman filtering to topography-mechanical decoupling

We propose the following gradient-based adaptive Kalman filter, presented in the discrete-time domain,

$$\begin{aligned} x(k) &= A[m]x(k-1) + B[m]u(k) + w(k) \\ y(k) &= C[m]x(k) + v(k), \qquad m = 1, \cdots, N_s \end{aligned} \tag{1}$$

where $G_{p2d}(j\omega, m) = \{A[m], B[m], C[m]\}$ is the dynamics from the input voltage to the z-axis piezo actuator to the cantilever deflection during the imaging-mapping process (when a stable probe-sample contact is maintained, i.e., the probe-sample contact is dominated by the repulsive force region), called the piezo-to-deflection dynamics below, N_s denotes the total sampling locations on one scan line, and $u(k)$, $w(k)$, and $v(k)$ are the excitation input signal (e.g., the injected PBE signal), the topography driven signal with the process noise, and the topography tracking signal with the measurement noise, respectively. The piezo-to-deflection dynamics, $G_{p2d}(j\omega, m)$, depends on the sample-probe interaction (contact), and thereby for heterogeneous materials, is location dependent in general. As for many polymer materials, the viscoelastic behavior is mainly presented in the frequency region much lower than the resonant frequency of the piezo-cantilever dynamics, the material-caused variation of the dynamics $G_{p2d}(j\omega, m)$ is mainly concentrated in the relatively low frequency region, i.e., the variation of $G_{p2d}(j\omega, m)$ is dominated by the change of the quasi-static gain of $G_{p2d}(j\omega, m)$ in the low frequency region, i.e.,

$$A[m] = A, \quad C[m] = C, \quad B[m] = B_n[m] \tag{2}$$

where $n = 1, \cdots, N_\ell$ is the n^{th} scan line in the total N_ℓ number of scan lines per image. Equivalently, we can consider $B[m] = B$, and $C[m] = C_n[m]$ instead.

As an example, the frequency responses of the piezo-to-deflection dynamics experimentally measured on a PDMS sample (with the Young's modulus around a few MPa) and an epoxy sample (with Young's modulus around a few hundreds of MPa) are compared in Fig. 3, respectively. It is evident that, within the measurement frequency range (2 kHz and below), the differences were mainly concentrated in the low frequencies (i.e., 10 Hz to 1,000 Hz).

Therefore, in the proposed gradient-based adaptive Kalman filtering technique, we focus on adaptive tuning of the input vector $B_n[m]$ line by line to accommodate the material, based on the gradient decent algorithm as

$$\begin{aligned} B_1[m] &= \rho_o \cdot S_1[m], \\ B_n[m] &= B_{n-1}[m] + \rho_g \cdot (S_n[m] - B_{n-1}[m]), \\ & \qquad n = 2, \cdots, N_\ell; \quad m = 1, \cdots, N_s \end{aligned} \tag{3}$$

where the subscript "n" in $B_n[m]$ denotes the n^{th} scan line, N_ℓ is the number of total scan lines (per image), $\rho_o > 0$ is a constant, ρ_g is the gradient scale factor, and $S_n[\cdot]$ is the so-called mechanical indicator on the n^{th} scan line, respectively. The mechanical indicator $S_n[\cdot]$ captures the spatial variation of the sample response at different sampling locations (under the same signal applied to the z-axis piezo). Next, we propose a compressed-sensing-based approach to obtain the mechanical indicator.

C. Mechanical indicator based on compressed sensing

The basic idea of the mechanical indicator stems from the observation that the spatial variation of the sample mechanical property can be quantified directly by using the cantilever deflection with the same z-axis piezo displacement, provided that the effect of the sample topography variation can be excluded. During the imaging-mapping process, however, such a cantilever deflection variation caused by the spatial nanomechanical fluctuation is mixed and coupled with that caused by the topography fluctuation, and it is challenging (if not completely impossible) to extract the material-caused deflection variation directly. We propose to obtain the mechanical indicator for the first scan line, $S_1[\cdot]$, offline a priori first, and then estimate the mechanical indicator for the rest of scan lines, $S_n[\cdot]$, by using the cantilever deflection on the preceding scan lines. The first-line mechanical indicator $S_1[\cdot]$ will be obtained via a compressed-sensing-based approach [22][23].

1) First-line mechanical indicator based on compressed sensing: To obtain the first-line mechanical indicator $S_1[\cdot]$, we measure the cantilever deflection at discrete sampling locations on the first scan line, by engaging the probe at each of the sampling locations to the same preload force level, applying the same z-axis piezo displacement (i.e., the z-axis piezo displacement follows the same excitation trajectory), withdrawing the cantilever, and transiting it to the next sampling location, and then repeating this process. As such, the change of the cantilever deflection between different locations shall be only caused by the difference of the material properties between those locations (within the acceptable measurement uncertainties). Although such a discrete measurement can be obtained by covering all the sampling locations on the first scan line, it is time consuming and low efficient. Thus, we propose to, based on the compressed-sensing theory, measure only at a small fraction of all the sampling locations (see Fig. 4), then optimally estimate/restore the cantilever deflection variation across all the chosen same-line discrete sampling locations [21].

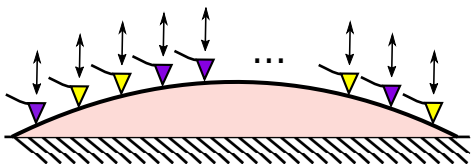

Fig. 4: A schematic representation of the compressed-sensing-based estimation of mechanical indicator, where the sample responses (i.e., the cantilever deflection) to the excitation force are measured at randomly-selected locations (marked by the purple probes) to estimate those at all the chosen discrete locations across the entire scan line (marked by the purple and the yellow probes).

Specifically, at the first scan line (we assume the x-axis is the scanning direction) a number of p sampling locations, $x_i, i = 1, 2, \cdots p$ (x_i: the x-coordinate of the i^{th} sampling location), are selected from a total number of q sampling locations on the same line, $x_j, j = 1, 2, \cdots, q$, where the p locations are obtained as the first p points of the random permutation of the total q sampling locations [24], i.e.,

$$\begin{aligned} & \hat{S} \subset S, \quad \text{with} \\ & \hat{S} = \{x_i | i = 1, 2, \cdots, p\} \text{ and} \\ & S = \{x_j | j = 1, 2, \cdots, q\} \end{aligned} \tag{4}$$

The coordinates in set $\hat{S}$ can be examined a priori and regenerated (if needed) such that the locations will not be particularly concentrated in any certain regions while leaving other regions sparsely covered. Then, the cantilever deflection measured at these p locations, $d_p[k]$, for $k = 1, 2, \cdots, p$, is utilized to recover/approximate the cantilever deflection over the total q number of sampling locations, $\hat{d}_q[i]$, for $i = 1, 2, \cdots, q$. An appropriate homomorphism transform (e.g., the Fourier transform) is chosen, such that the data are sparse in the transformed domain, i.e., choose a transform $\mathcal{T}$

$$d_p(\cdot) \xrightarrow{\mathcal{T}} \chi_p(\cdot), \quad \hat{d}_q(\cdot) \xrightarrow{\mathcal{T}} \chi_q(\cdot) \tag{5}$$

such that χ_p will be sparse.

Then, the cantilever deflection on all the q number of sampling locations, $\hat{d}_q[\cdot]$, is recovered by minimizing the ℓ_1 norm of the estimated signal $\hat{d}_q[\cdot]$ in the transformed domain, χ_q,

$$\begin{aligned} & \text{minimize} \quad \|\chi_q\|_1 \\ & \text{subject to} \quad d_p(\cdot) = \Phi \hat{d}_q(\cdot) = \Phi\Psi\chi_q(\cdot) \end{aligned} \tag{6}$$

where $\Phi \in \Re^{p\times q} : \Re^{p\times 1} \rightarrow \Re^{q\times 1}$ is a sparse matrix with entries equaling to 0 or 1 that specifies the sampling (spatial) locations of each measured deflection data $\hat{d}_p(k)$ in the full vector of deflection $\hat{d}_q(k)$ for $k = 1, \cdots p$, i.e., Φ is the mapping from S to $\hat{S}$, and $\Psi \in \Re^{q\times q} : \Re^{q\times 1} \rightarrow \Re^{q\times 1}$ is the sparsity basis corresponding to the chosen inverse transform $\mathcal{T}^{-1}$, respectively.

The above algorithm is summarized in Algorithm 1 below.

Algorithm 1 Compressed-sensing based estimation of the spatial nanomechanical fluctuation on AFM

- Randomly choose the measurement positions as a subset $\hat{S}$ from a set S of all the sampling locations;
- Conduct the required measurements at each location specified in set $\hat{S}$;
- Transform the measured results at locations of set $\hat{S}$ to a sparse space;
- Recover the measured results for all the locations in set S by solving the ℓ_1 minimization in Eq. (6).

In this work, discrete cosine transform (DCT) [25] is chosen as the homomorphism transform in the above compressed sensing scheme,

$$\chi_p(n) = \sqrt{\frac{2}{p}} \sum_{k=1}^{p} d_p(k) \frac{1}{\sqrt{1+\delta_{k1}}} \cos(\frac{\pi}{2p}(k-1)(2n-1)), \quad \text{for } k = 1, \cdots, p, \text{ and } n = 1, 2, \cdots, p \tag{7}$$

where δ_{k1} denotes the Kronecker delta.

2) Mechanical indicator on the rest of scan lines: The mechanical indicator on the rest of scan lines, $S_n[\cdot]$, for $n = 2, \cdots, N_\ell$, can be obtained based on that of the first line quantified above, provided that the difference of the mechanical distribution of the sample across two successive scan lines is small. This condition is reasonable and widely holds in practices as the spatial variation of the mechanical properties of most soft materials is continuous across the sample area, and the increment of the line-to-line distance can be rendered small by increasing the number of scan lines. Thus, the mechanical indicator on the subsequent scan lines can be approximated as proportional to the cantilever deflection responses to the PBE signal on the previous scan lines, i.e.,

$$\begin{aligned} S_n[m] &= k_s \max_k d_{ind,n-1}[m], \quad \text{with} \\ S_1[m] &= k_s \hat{d}_q(m), \quad , m = 1, 2, \cdots, N_s \end{aligned} \tag{8}$$

where k_s is a constant that converts the cantilever deflection to the indicator, and $\max_k d_{ind,n-1}[m]$ denotes the moving maximum of the cantilever deflection response with a window of k points, i.e.,

$$\max_k d_{ind,n}[m] = \max_{i=m-k+1,\cdots,m} d_{ind,n}[i] \tag{9}$$

The moving average is used to smooth out short-term fluctuations (i.e. the measurement noise).

D. Sample topography tracking and quantification

Once the response to the PBE signal is decoupled from that to the sample topography via the above adaptive Kalman filtering, the decoupled cantilever response and the z-sensor displacement will be utilized to estimate the sample topography and the indentation generated (due to the PBE excitation applied) for nanomechanical mapping. Basically, the sample deformation generated during the imaging will be online estimated based on the recently developed control-based nanomechanical measurement technique (CINM) [26], and accounted for in the quantification of the sample topography. Then the sample topography will be tracked by using a data-driven online iterative-learning feedforward control augmented to the z-axis feedback control loop, as developed in the adaptive contact-mode imaging [27]. The readers are referred to [15] for details.

III. Experimental Example

In this section, the proposed A-SIBNM technique is demonstrated by implementing it in experiments.

A. Experiment setup

The experiments were conducted on a commercial AFM system (Dimension FastScan, Bruker Inc.) on which direct access to the piezoelectrical actuators and the corresponding displacement and cantilever deflection sensor signals were provided. The algorithm to implement the A-SBINM technique was designed in Matlab-Simulink and implemented via a data acquisition system (PCI-6259, National Instruments) under xPC-target real-time operation system. The sampling rate of all experiments was set at 10 kHz due to the hardware limitation.

A PDMS-epoxy sample of heterogeneous mechanical properties was used in the experiments. The sample was prepared by partially filling an epoxy pentagonal quasicrystal with 1 μm characteristic length scale (in yellow color in Fig. 5) with crosslinked PDMS material (in green/blue color in Fig. 5). Specifically, the epoxy quasicrystal pattern was made by thermal microembossing [28] of an SU-8 2015 (MicroChem) thin film. The film was deposited by spin coating onto a glass slide and embossed at 95 °C with a silicone stamp that was made with a silicon master of the quasicrystal pattern. After embossing, the film was crosslinked by lengthy flood UV exposure and a dilute solution of Sylgard 184 silicone (Dow Chemical) in hexane (Sigma Aldrich) was drop cast onto it. After curing of the silicone by lengthy baking at 70 °C, a region near the edge of the drop where the pattern was only partially filled was identified. The elastic modulus of the PDMS and the epoxy material used were around 500 kPa and 50 MPa, respectively.

B. Implementation of the A-SIBNM technique

First, the z-piezo dynamics $G_{pz}(j\omega)$ and the piezo-to-deflection dynamics $G_{p2d}(j\omega)$ were measured and identified by applying a band-limited broadband white noise to drive

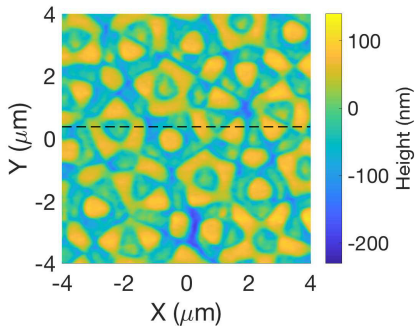

Fig. 5: AFM image (contact-mode, at scan rate of 1 Hz) of the PDMS-epoxy sample used in the experiment, where the material of the yellow patterns and the blue/green layer were epoxy and PDMS, respectively.

the z-axis piezo actuator (after a stable probe-sample contact was established with the preload force 2 times larger than the amplitude of the white-noise force), and measuring, respectively, the z-displacement and the cantilever deflection as the output. The measurements were obtained at the first imaging-mapping position of the PDMS-epoxy sample without lateral displacements. Then a state-space model of the obtained z-piezo dynamics and that of the piezo-to-deflection dynamics were obtained by using the system identification toolbox in Matlab, and used to design the Kalman filter and the adaptive Kalman filter applied to decouple the z-axis sensor signal and the cantilever deflection, respectively [15].

Next, to design the adaptive Kalman filter, the compressed-sensing-based method to obtain the first-line mechanical indicator was implemented to quantify the spatial variation of the cantilever deflection on the first scan line. A multi-sinusoidal signal $V_e(t)$ consisting of 10 equispaced frequency components between 100 Hz and 1,000 Hz was applied to the z-axis piezo actuator as the PBE signal,

$$V_e(t) = \sum_{k=1}^{10} \sin(200\pi kt) \quad t \in [0,\ 0.01] \text{ sec}, \qquad (10)$$

then the cantilever deflection was measured at 25 random locations of a total 51 sampling locations on the first scan line as described in Sec. II.

The cantilever deflection measured at the 25 randomly chosen locations was then used to obtain the mechanical indicator on the first scan line. Specifically, the maximum amplitude of the cantilever deflection responses to the PBE signal $V_e(t)$ in eq. (10) at the 25 randomly chosen locations were used as the mechanical indicator, i.e., $d_{25}[k] = \|d_{25,k}(\cdot)\|_\infty$, for $k = 1, 2, \cdots, 25$. Then, the vector of $d_{25}[\cdot]$ was transformed to the sparse domain of the IDCT in eq. (7). The full vector of $d_{51}[\cdot]$ at all the 51 sampling locations on the first scan line was recovered/approximated by applying the ℓ_1 optimization in eq. (6) by using the measured value of $d_{25}[\cdot]$. Finally, the first-scan-line mechanical indicator was generated by normalizing the recovered vector $\hat{d}_{51}[\cdot]$ with its first value, i.e., $\hat{d}_{51}[k] = \hat{d}_{51}[k]/\hat{d}_{51}[1]$, for $k = 1, \cdots, 51$. This guarantees that the Kalman input gain $B[m]$ changes from 1.

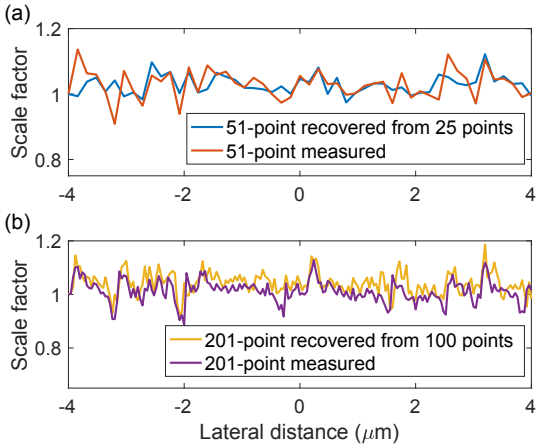

Fig. 6: Mechanical indicator of the sample points on the first scan line recovered by using the compressed sensing technique at different number of sampling locations.

Finally, the above obtained mechanical indicator was used in the gradient-based adaptive Kalman filter to implement the adaptive SIBNM technique, by updating the gain of the Kalman filter line by line. A multiple sinusoidal signal $V_e(t)$ consisting of 10 equispaced frequency components from 100 Hz to 1,000 Hz was injected as the PBE excitation input.

In the experiments, a sample area of 8 μm $\times$ 8 μm was mapped with a total of 250 scan lines. Given the hardware limitation and to maintain the same lateral resolution in both the x- and y- axes direction, the measured force and indentation over every 100 sampling locations were averaged to represent the mechanical property in each sampling area of 0.16 μm by 0.16 μm size, i.e., the lateral resolution was 0.16 μm in both the x- and y- axis direction, respectively—The lateral resolution of the nanomechanical mapping can be increased proportionally by improving the closed-loop sampling rate accordingly. The averaged measured indentation and force signals were used to compute the complex modulus via the following Hertzian contact model [29]:

$$E^*(j\omega) = \frac{F(j\omega)}{2RI(j\omega)} \qquad (11)$$

where $F(j\omega)$ and $I(j\omega)$ denote the force applied to the sample (e.g., in this study, the force generated by the multi-sinusoidal input) and the corresponding indentation generated, respectively, and R is the radius of the AFM tip ($R = 25$ nm), respectively. A relatively soft cantilever (model: DNP-10, Bruker Nano Inc., spring constant around 0.2 N/m) was used, and the lateral scan rate was kept at 1 Hz due to the control hardware limitation. The lateral scan rate can be further increased by increasing the sampling rate.

C. Experiment results and discussion

The compressed-sensing-based estimation of the mechanical indicator on the first scan line was tested first. The recovered results obtained by using two different compression ratio: the 51-point mechanical indicator recovered from the

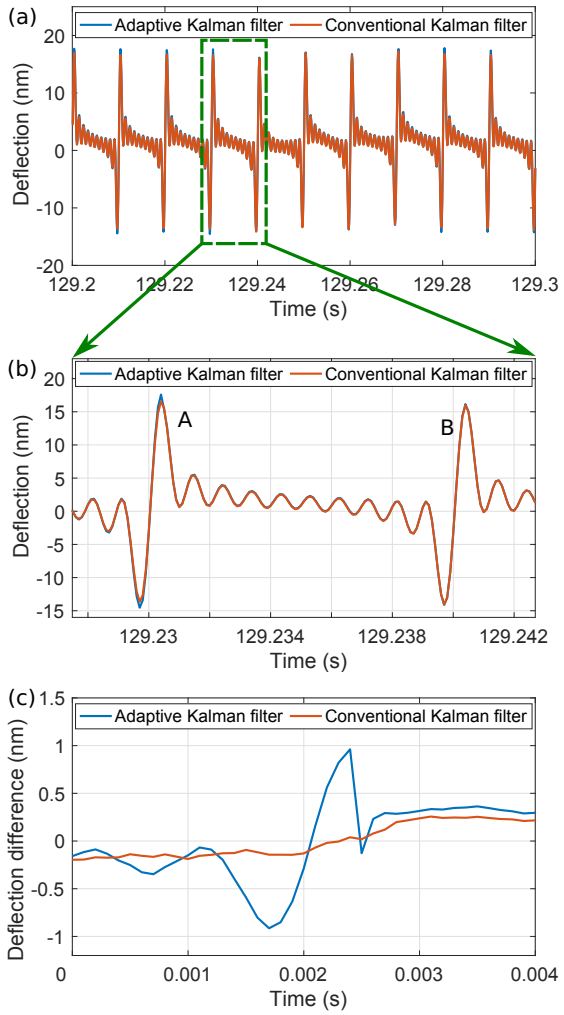

Fig. 7: (a) Comparison of the decoupled PBE-caused cantilever deflection response obtained by using the proposed adaptive Kalman filter to that by using the conventional Kalman filter, respectively, (b) the zoomed-in view of the comparison, and (c) the difference of the cantilever deflection response at location "A" and location "B" by using adaptive Kalman filter (blue) and the conventional Kalman filter (red), respectively.

25-point measured data, and the 201-point one recovered from the 100-point measured data, are compared in Fig. 6.

First, the experimental results showed that the mechanical indicator can be captured with the 51-point measured data (see red-line plot in Fig. 6(a)). The accuracy of the mechanical indicator can be further improved by measuring at more locations, i.e., more details were captured with the 201-point measured mechanical indicator (the purple-line plot in Fig. 6(b)) than the 51-point measured mechanical indicator. Secondly, by using compressed sensing method, the mechanical indicator can be recovered, as both the trend and the value of the corresponding measured mechanical indicator were captured by the recovered indicator in both 25-to-51 and 100-to-201 cases. Both the 25-to-50 point recovered mechanical indicator (the blue line in Fig. 6) and the 100-to-201 point recovered mechanical indicator (the yellow line in Fig. 6) captures the feature of their "true" ones (i.e., the 51-point one in the red line and the 201-point one in violet line in Fig. 6), respectively. And the correlation between the 100-to-201 point recovered indicator and its "true" one at 0.5883 was larger than that between the 25-to-51 point recovered one and its "true" one at 0.4703. Both the accuracy of the recovery and the compression ratio can be further improved as the number of total sampling locations increases. More sampling locations are needed when the entire imaging/mapping area becomes relatively large (e.g., a live mammalian cell of size over 90 μm $\times$ 90 μm). Save of the first-line measurement time gained via the proposed compressed sensing method also becomes more pronounced when the measurement time at each sampling location becomes large (e.g., on live cell). Therefore, the experimental results demonstrated the capability of the proposed compressed-sensing-based in capturing the mechanical distribution over the sample surface.

Next, the efficacy of the adaptive Kalman filter in decoupling and splitting the two responses (i.e., the response to the topography variation and the PBE input, respectively) was assessed, with comparison to the conventional Kalman filter. The decoupled cantilever deflection response to the applied PBE signal (see eq. (10)) obtained by using the adaptive Kalman filter was compared to that obtained by using the conventional Kalman filter in Fig. 7. Due to the hardness difference of the two materials in the PDMS-epoxy sample, the amplitude of the decoupled PBE-caused cantilever deflection should be larger around the hard-portion of the sample, i.e., the epoxy portion (e.g., location "A" in Fig. 5), than that around the soft-portion, i.e., the PDMS portion (e.g., location "B" in Fig. 5) of the sample (for the sample amplitude of PBE input). Such a material-dependent deflection variation was clearly captured by using the adaptive Kalman filter: As shown in Fig. 7(b) and Fig. 7(c), the amplitude of the second peak (at location "B" in Fig. 5) obtained by using the A-SIBNM was reduced by 6.92% from the first peak (at location "A" in Fig. 5), whereas the amplitude of the two peaks obtained by using the SIBNM were almost the same. Specifically, the A-B deflection difference obtained by using the adaptive Kalman fitler was at least two times larger than that by the conventional one (see Fig. 7 (c)). Therefore, the experimental results demonstrated that the proposed gradient-based adaptive Kalman filtering method can capture the spatial mechanical variations during the simultaneous imaging-mapping process.

The experimental results showed that with the proposed A-SIBNM technique, the topography imaging of the heterogeneous sample can be reliably acquired, as shown in Fig. 8. The pentagon feature of the PDMS-epoxy sample topography was clearly captured—the image quality was compared well to that obtained by the conventional contact-mode imaging (compare Fig. 5 to Fig. 8). Specifically, the sample height difference quantified by using the proposed A-SIBNM method at around 100 nm was close to that quantified by using the contact-mode imaging. Sample topography profiles along the

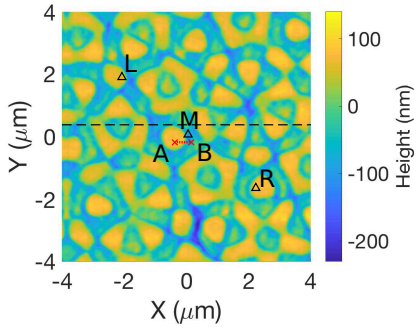

Fig. 8: The topography image of the PDMS-epoxy sample acquired by the proposed A-SIBNM technique, where the red-dashed line denotes the location where the cantilever deflection comparison results shown in Fig. 7 were taken, with "A" and "B" corresponding to the two peaks shown in Fig. 7(b), respectively, and "L", "M", and "R" denote three random locations at which the complex modulus was measured by using the CINM method at that point (without scanning) and compared to those obtained by using the proposed A-SIBNM technique, as shown in Fig. 11, respectively.

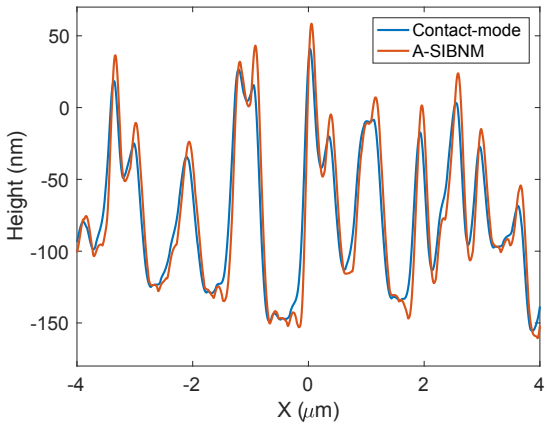

Fig. 9: Comparison of the cross-section sample topography profiles at randomly-chosen scan lines (black dashed lines) in Fig. 5 by contact-mode imaging and Fig. 8 by A-SIBNM technique, respectively.

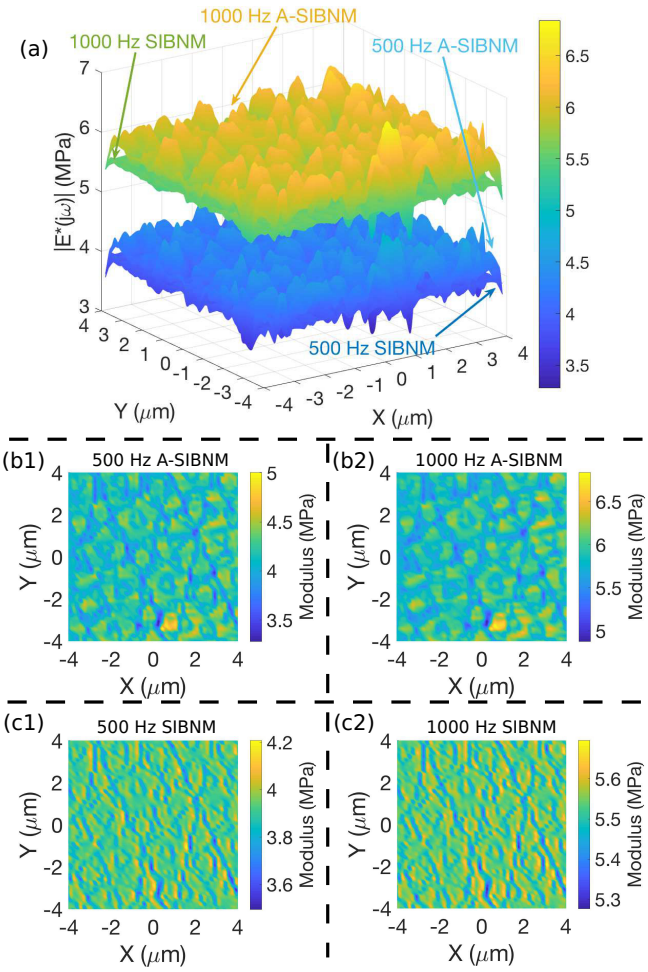

Fig. 10: Mechanical mapping of the PDMS-Epoxy sample at measurement frequency of 500 Hz and 1000 Hz by using the A-SIBNM technique, compared to those obtained by using the SIBNM technique, respectively: (a) 3-D mapping, (b1) mapping at 500 Hz by the A-SIBNM technique, (b2) mapping at 1000 Hz by the A-SIBNM technique, (c1) mapping at 500 Hz by the SIBNM technique, and (c2) mapping at 1000 Hz by the SIBNM technique, respectively.

cross-sections in Fig. 5 and Fig. 8 are presented in Fig. 9.

The experimental results also demonstrated that the frequency-dependent mechanical mapping of the PDMS-epoxy sample can be clearly quantified by using the proposed A-SIBNM approach. The mapping of the amplitude of the complex modulus over the sampling area obtained by using the A-SIBNM technique is compared to that obtained by using the SIBNM method in Fig. 10(a). Firstly, the modulus mappings obtained by both methods at 1000 Hz were above those at 500 Hz, signaling the increase of the elastic modulus of polymers with an increase of the excitation frequency, agreed with the characteristics of the viscoelasticity of polymers [4][30][31]. Secondly, the mechanical patterns of the pentagon feature—due to the material difference between the PDMS filled-up (in blue/green color in the topography image in Fig. 8) and the epoxy pentagon pattern (in yellow color in Fig. 8)—were clearly captured by using the proposed A-SIBNM technique, and became more pronounced as the frequency increased. More specifically, the change (increase) of the modulus between the lower filled-up layer to the intermediate layer, i.e., between the bottom blue layer and the intermediate green layer in the topography image in Fig. 8, was less pronounced to that between the filled-up layer and the pentagon pattern, i.e., between the green layer and the yellow pattern in Fig. 8, even though the corresponding topography difference between the former (i.e., between the blue- and the green- layer) was twice larger than the latter (i.e., between the green layer and the yellow pattern). Such a difference agreed to our prediction as the two filled-up layers

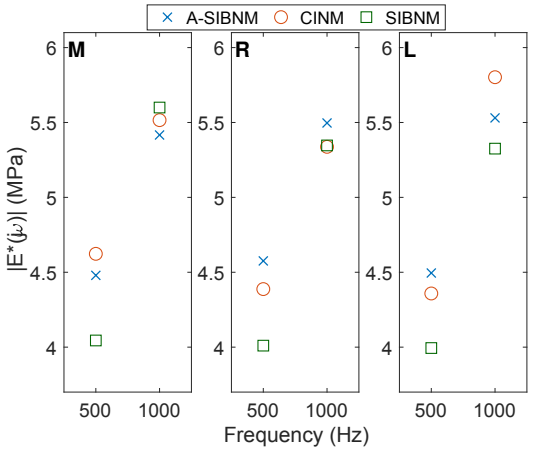

Fig. 11: Comparison of the amplitude of the complex modulus obtained by using the A-SIBNM technique to those obtained by using the CINM technique without scanning at the three randomly-selected locations (marked as "M", "L", and "R" in Fig. 8), respectively.

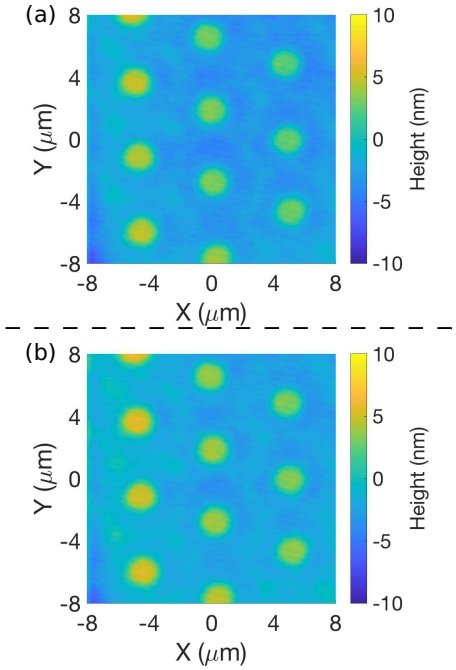

Fig. 12: The topography image of the SU-8 sample obtained by using (a) contact-mode imaging at scan rate of 1 Hz, and (b) the proposed A-SIBNM technique, where the material of the yellow patterns and the blue layer were the laser treated part and untreated part, respectively.

were mainly composed by PDMS, whereas the pentagon patterns were mainly composed by epoxy instead. However, such a mechanical characteristics of the sample was not well captured by using the SIBNM method. As shown in Fig. 10(c1) and Fig. 10(c2), the pentagon features were much less clear and less regular in the mapping obtained by the SIBNM technique, and the material-caused change of the modulus was not well quantified—the increase of the modulus was captured at the edges of the pentagon patterns only, not across the whole patterns as it should be (see Fig. 10(b1) and Fig. 10(b2)). Therefore, the experimental results demonstrated that capability of the proposed A-SIBNM technique in quantitatively capturing the mechanical distribution of heterogeneous materials.

To further evaluate the mechanical mapping obtained by the A-SIBNM technique, we also measured the complex modulus of the sample at three randomly-selected locations of the sample by using the CINM method, and compared the results with those obtained by using the A-SIBNM technique. The cantilever probe was positioned to each of the three locations (marked as "M", "L", and "R" in Fig. 8) to measure the modulus at that location by using the CINM method directly, and then repositioned to the next location– In this point-by-point measurement without scanning, the effect of the sample topography variation on the mechanical property measurement was avoided, and the modulus obtained can be utilized as the reference. The mechanical mapping/measurement by using the ASIBNM technique and the CINM technique at these three different sample locations are compared in Fig. 11. The comparison showed that the value of the complex modulus acquired by the proposed A-SIBNM technique were close to those by the CINM method—among the three selected locations, the relative difference (with respect to the values obtained by the CINM method) was between 3.1% and 4.3% for modulus at 500 Hz, and between 1.8% and 4.9% for modulus at 1000 Hz, respectively (see Fig. 11). The use of the CINM technique in quantifying the complex modulus of soft materials including polymers has been demonstrated previously [26][29][31]. Thus, this comparison also showed that through the proposed A-SIBNM technique, both the sample topography and nanomechanical distribution of heterogeneous materials can be decoupled and simultaneously quantified.

To further test and evaluate the proposed A-SIBNM technique, a plasticized SU-8 epoxy photoresin sample of different topography characteristics (see Fig. 12) was also imaged/mapped over an area four times larger (16 μm $\times$ 16 μm) than the above. The SU-8 sample was prepared by plasticizing through addition of Epon 815c low viscosity epoxy resin until a desired softness of 4 MPa was achieved, and then focused laser exposure was applied in a hexagonal array of point exposures to crosslink the material at these positions. The Epon 815c possessed glycidyl functionality to participate in the SU-8 epoxide crosslinking, but no photosensitive chemistries of its own. As a result, the photocrosslinking was subtle enough to remain after solvent development (shown in Fig. 13(a)), but resulted in a very low small change in mechanical stiffness. Thus, this sample served well to assess the performance of a SIMM technique in discerning such a subtle mechanical distribution while imaging the sample topography simultaneously.

The sample was imaged-mapped at the scanning rate of 1 Hz, where a multi-sinusoidal signal consisting of two fre-

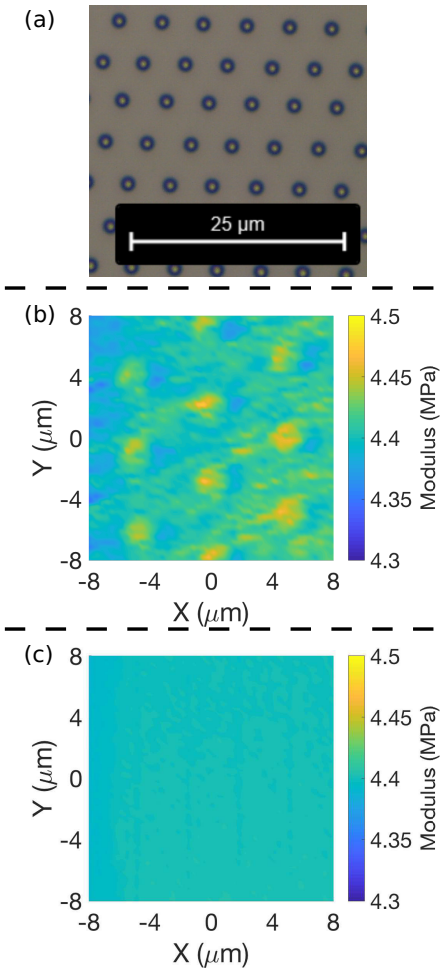

Fig. 13: Analysis of a plasticized SU-8 sample. (a) An optical microscope image of a sample e mapped sample in (b,c), but after rinsing in a photoresist developer (propylene glycol monomethyl ether acetate, Sigma Aldrich $> 99\%$). (b,c) Mechanical mapping of the SU-8 sample at measurement frequency of 500 Hz by using the A-SIBNM technique, compared to the result obtained by using the SIBNM technique, respectively: (b) mapping at 500 Hz by the A-SIBNM technique, and (c) mapping at 500 Hz by the SIBNM technique, respectively.

quency components from 100 Hz to 1000 Hz and amplitude of 0.3 V was applied as the PBE excitation input. The topography image and the mechanical mapping obtained are shown in Fig. 12 and Fig. 13(b), respectively. For comparison, the mechanical mapping was also obtained by using the SIBNM method, as shown in Fig. 13(c). That such small mechanical differences could be detected speaks to the capabilities of this method.

The experimental results on the SU-8 sample, indeed, further demonstrated the performance and capability of the proposed A-SIBNM technique. As shown in Fig. 12, the topography image acquired by the proposed A-SIBNM technique compared well to the contact-mode imaging result– visually there was no noticeable difference. Moreover, the mechanical mapping result (in top-view) of the SU-8 sample obtained by the A-SIBNM technique showed that the heterogeneous property of the SU-8 sample was clearly captured. Specifically, the dots part in the topography result (Fig. 12) with large mechanical property was clearly reflected in the modulus mapping (Fig. 13(b)). However, there was not discernible mechanical variations in the mapping result obtained by the SIBNM technique (Fig. 13(c)). Therefore, that such small mechanical differences could be detected—with simultaneous topography imaging—spoke directly to the capabilities of the proposed A-SIBNM technique.

IV. Conclusion

In this paper, an adaptive Kalman-filtering-based approach has been proposed to achieve simultaneous topography imaging and nanomechanical mapping of heterogeneous soft materials (A-SIBNM). First, a gradient based method was proposed to adaptively adjust the gain of the Kalman filter online to accommodate the spatial variations of the sample mechanical properties during the scanning. Next, to characterize the cantilever deflection variation due to the heterogeneous mechanical variations of the sample, a compressed-sensing-based technique was proposed to obtain the indicator function efficiently that was utilized to adaptively adjust the gain of the Kalman filter. The proposed approach was implemented on a polydimethylsiloxane-epoxy (PDMS-epoxy) sample and a plasticized SU-8 epoxy photoresin sample of pronounced topography variation and heterogeneous mechanical properties. The experimental results obtained showed that both the topography imaging and the qualitative broadband mechanical mapping of heterogeneous soft samples can be reliably quantified by the proposed A-SIBNM technique.

Acknowledgment

T. Li and Q. Zou would like to gratefully thank the support of NSF grants IDBR-1353890, CMMI-1663055 and CMMI-1923856.

References

[1] Leo Gross, Fabian Mohn, Nikolaj Moll, Peter Liljeroth, and Gerhard Meyer. The chemical structure of a molecule resolved by atomic force microscopy. *Science*, 325(5944):1110–1114, 2009.

[2] Emilios K Dimitriadis, Ferenc Horkay, Julia Maresca, Bechara Kachar, and Richard S Chadwick. Determination of elastic moduli of thin layers of soft material using the atomic force microscope. *Biophysical journal*, 82(5):2798–2810, 2002.

[3] Sarah E Cross, Yu-Sheng Jin, Jianyu Rao, and James K Gimzewski. Nanomechanical analysis of cells from cancer patients. *Nature nanotechnology*, 2(12):780, 2007.

[4] Juan Ren, Shiyan Yu, Nan Gao, and Qingze Zou. Indentation quantification for in-liquid nanomechanical measurement of soft material using an atomic force microscope: Rate-dependent elastic modulus of live cells. *Physical Review E*, 88(5):052711, 2013.

[5] Subhadip Senapati and Stuart Lindsay. Recent progress in molecular recognition imaging using atomic force microscopy. *Accounts of chemical research*, 2016.

[6] Marius Chyasnavichyus, Seth L Young, and Vladimir V Tsukruk. Probing of polymer surfaces in the viscoelastic regime. *Langmuir*, 30(35):10566–10582, 2014.

[7] Jozef Adamcik, Alexandre Berquand, and Raffaele Mezzenga. Single-step direct measurement of amyloid fibrils stiffness by peak force quantitative nanomechanical atomic force microscopy. *Applied Physics Letters*, 98(19):193701, 2011.

[8] A Rosa-Zeiser, E Weilandt, S Hild, and O Marti. The simultaneous measurement of elastic, electrostatic and adhesive properties by scanning force microscopy: pulsed-force mode operation. *Measurement Science and Technology*, 8(11):1333, 1997.

[9] Bede Pittenger, Natalia Erina, and Chanmin Su. Quantitative mechanical property mapping at the nanoscale with peakforce qnm. *Application Note Veeco Instruments Inc*, pages 1–12, 2010.

[10] M Radmacher, RW Tillmann, and HE Gaub. Imaging viscoelasticity by force modulation with the atomic force microscope. *Biophysical journal*, 64(3):735–742, 1993.

[11] Masaru Arai, Eijun Ueda, Xiaobin Liang, Makiko Ito, Sungmin Kang, and Ken Nakajima. Viscoelastic maps obtained by nanorheological atomic force microscopy with two different driving systems. *Japanese Journal of Applied Physics*, 57(8S1):08NB08, 2018.

[12] Bede Pittenger, Sergey Osechinskiy, Dalia Yablon, and Thomas Mueller. Nanoscale dma with the atomic force microscope: A new method for measuring viscoelastic properties of nanostructured polymer materials. *JOM*, 71(10):3390–3398, 2019.

[13] A Gannepalli, DG Yablon, AH Tsou, and R Proksch. Mapping nanoscale elasticity and dissipation using dual frequency contact resonance afm. *Nanotechnology*, 22(35):355705, 2011.

[14] Jason P Killgore, DG Yablon, AH Tsou, A Gannepalli, PA Yuya, JA Turner, R Proksch, and DC Hurley. Viscoelastic property mapping with contact resonance force microscopy. *Langmuir*, 27(23):13983–13987, 2011.

[15] Tianwei Li and Qingze Zou. Simultaneous topography imaging and broadband nanomechanical mapping on atomic force microscope. *Nanotechnology*, 28(50):505502, 2017.

[16] Ozgur Sahin and Natalia Erina. High-resolution and large dynamic range nanomechanical mapping in tapping-mode atomic force microscopy. *Nanotechnology*, 19(44):445717, 2008.

[17] Pavel Trtik, Josef Kaufmann, and Udo Volz. On the use of peak-force tapping atomic force microscopy for quantification of the local elastic modulus in hardened cement paste. *Cement and concrete research*, 42(1):215–221, 2012.

[18] Abu Sebastian, Deepak R Sahoo, and Murti V Salapaka. An observer based sample detection scheme for atomic force microscopy. In *Decision and Control, 2003. Proceedings. 42nd IEEE Conference on*, volume 3, pages 2132–2137. IEEE, 2003.

[19] Michael G Ruppert, Kai S Karvinen, Samuel L Wiggins, and SO Reza Moheimani. A kalman filter for amplitude estimation in high-speed dynamic mode atomic force microscopy. *IEEE Transactions on Control Systems Technology*, 24(1):276–284, 2016.

[20] Eric A Wan and Rudolph Van Der Merwe. The unscented kalman filter for nonlinear estimation. In *Adaptive Systems for Signal Processing, Communications, and Control Symposium 2000. AS-SPCC. The IEEE 2000*, pages 153–158. Ieee, 2000.

[21] David L Donoho. Compressed sensing. *IEEE Transactions on information theory*, 52(4):1289–1306, 2006.

[22] Tobias Lindstrøm Jensen, Thomas Arildsen, Jan Ostergaard, and Torben Larsen. Reconstruction of undersampled atomic force microscopy images: Interpolation versus basis pursuit. In *2013 International Conference on Signal-Image Technology & Internet-Based Systems*, pages 130–135. IEEE, 2013.

[23] Emmanuel Candes and Justin Romberg. l1-magic: Recovery of sparse signals via convex programming. *URL: www. acm. caltech. edu/l1magic/downloads/l1magic. pdf*, 4:14, 2005.

[24] Emmanuel J Candes. The restricted isometry property and its implications for compressed sensing. *Comptes rendus mathematique*, 346(9-10):589–592, 2008.

[25] Nasir Ahmed, T_ Natarajan, and Kamisetty R Rao. Discrete cosine transform. *IEEE transactions on Computers*, 100(1):90–93, 1974.

[26] Juan Ren and Qingze Zou. A control-based approach to accurate nanoindentation quantification in broadband nanomechanical measurement using scanning probe microscope. *IEEE Transactions on Nanotechnology*, 13(1):46–54, 2014.

[27] Juan Ren and Qingze Zou. High-speed adaptive contact-mode atomic force microscopy imaging with near-minimum-force. *Review of Scientific Instruments*, 85(7):073706, 2014.

[28] Stephen Y Chou, Peter R Krauss, and Preston J Renstrom. Imprint of sub-25 nm vias and trenches in polymers. *Applied physics letters*, 67(21):3114–3116, 1995.

[29] Juan Ren, Aliyeh Mousavi, Xuemei Li, Qingze Zou, Natalia Erina, and Chanmin Su. Enhanced measurement of broadband nanomechanical property of polymers using atomic force microscope. *Applied Physics Letters*, 102(18):183116, 2013.

[30] Thomas G Mason and DA Weitz. Optical measurements of frequency-dependent linear viscoelastic moduli of complex fluids. *Physical review letters*, 74(7):1250, 1995.

[31] Zhonghua Xu, Kyongsoo Kim, Qingze Zou, and Pranav Shrotriya. Broadband measurement of rate-dependent viscoelasticity at nanoscale using scanning probe microscope: Poly (dimethylsiloxane) example. *Applied Physics Letters*, 93(13):133103, 2008.